Testing radiation-driven wind theory at low metallicity with the O dwarf LP26

Ciarán Furey*, Frank Backs, Prof. dr. Alex de Koter

Anton Pannekoek Institute for Astronomy,
University of Amsterdam, Science Park 904, 1098 XH Amsterdam, The Netherlands

Submitted 9 June, 2023.

Abstract

It is thought that the first generation of stars, Population III stars, were massive and metal free, and that they played a significant role in the reionisation of the Universe. However, directly observing these stars is not possible with current technology. Therefore, nearby massive, extremely metal poor stars (XMPs; $Z/Z_\odot \lesssim 0.05$) are studied to infer the nature of Population III stars. The determination of the mass-loss rate ($\dot{M}$) of these XMPs would provide useful tests of the current theory of the physics of stellar winds (radiation-driven wind theory; RDWT) as well as inform us how Population III stars may have contributed to the epoch of reionisation. In this report, we present the lowest metallicity test of RDWT to date. We analyse the FUV spectrum of XMP LP26 ($Z \sim 0.03\ Z_\odot$) located in the dIrr galaxy Leo P. Using the NLTE stellar atmosphere code FASTWIND, we model the C III λ1176 line and determine optimal parameters for LP26 by means of a grid-search approach using chi-squared minimisation. This results in a number of optimal models with different surface carbon abundances, surface gravities, and effective temperatures. Upper limits of $\dot{M}$ for these optimal models are then calculated using the C IV λ1550 line and are compared to a number of theoretical predictions. However, a degeneracy between effective temperature and surface gravity is found. To break this, we compare the optimal models to stellar evolutionary tracks, which allows us to rule out a number of possible models. We find that theory successfully predicts values for $\dot{M}$ below the calculated upper limits of the most optimal model. Although only two lines were analysed in this work, these results are promising and should motivate future work on other XMPs.

1. Introduction

After the formation of the Cosmic Microwave Background (CMB) at redshift $z \sim 1100$, the baryonic matter of the Universe consisted almost entirely of neutral H and He. Dark matter halos then formed, which captured this neutral gas to form the first stars, the so-called Population III stars (Wise, 2019). These Population III stars were extremely massive (Hirano et al., 2014), hot, and luminous, and therefore produced copious amounts of ionising radiation. This radiation, along with contributions from other sources, eventually lead to the complete reionisation of the intergalactic medium (IGM).

By observing 67 different quasar sightlines, Bosman et al. (2022) determined that a uniformly IGM appeared by $z = 5.3$, or $\sim 1.1\,\mathrm{Gyr}$ after the Big Bang. However, it is still not known for certain what exactly contributed to this reionisation, and by how much. By studying nearby extremely metal poor (XMP) O-type stars, we can learn more about how Population III stars partook in this epoch of reionisation, because, due to their low metallicities (Z), these XMPs may be representative of Population III stars, since they are also expected to be metal poor, or even metal free.

Of great interest is the mass loss rate ($\dot{M}$) of these

---

*Student number: 14182645; email: ciaran.furey@student.uva.nl

XMPs, and for a few reasons. Firstly, the determination of $\dot{M}$ at such low Z will provide useful tests of our current theory of how stars produce radiation-driven winds (radiation-driven wind theory; RDWT; Castor et al., 1975; see Vink, 2022, for a review). This theory states that stellar winds are caused by the transfer of momentum from radiation produced by the star to the elements in the atmosphere when light is absorbed in a spectral line. Verification of this theory will have profound implications for our understanding of stellar evolution as a whole, both at early cosmic time and in the present-day Universe, as well as the cumulative effect of evolution in stellar populations, modelled by means of stellar population synthesis codes.

Furthermore, mass loss results in the feedback of matter from the star into its surrounding interstellar medium (ISM) and beyond. Therefore, by knowing how XMPs inject material into their ISM, we can gain an insight into how Population III stars may have interacted with their ambient medium, and in what way they contributed to the reionisation of the Universe.

Fortunately, there exist metal poor galaxies in the Local Group that make the study of XMPs possible. Nearby, there are the Large and Small Magellanic clouds (LMC and SMC, respectively) whose metal content are one half and one fifth that of the Milky Way (Mokiem et al., 2007). Several other dwarf galaxies have an even lower metal content. One such galaxy is the dIrr Leo P, at a distance of (1.62 ± 0.15) Mpc (McQuinn et al., 2015). By using the [O III] $I(\lambda\lambda 4959, 5007)/I(\lambda 4363)$ ratio from a nebular emission source in Leo P, Skillman et al. (2013) determined an oxygen abundance of $12+\log(\text{O/H}) = 7.17 \pm 0.04$, or $Z/Z_\odot \simeq 1/30$, making it the most metal poor galaxy in the Local Group. The source of this nebular emission is a single O-type star: LP26.

Telford et al. (2021) performed spectral energy distribution (SED) fitting of this star using its FUV spectrum and archival Hubble Space Telescope (HST) infrared (IR) photometry to determine physi-

cal properties, such as the effective temperature, T_{eff}, surface gravity, g, and radius, $R_\star$, among others, and find values consistent with an O dwarf spectral type. Telford et al. (2023) determine the ratio of helium- and hydrogen-ionising photon production rate, and constrain T_{eff} for LP26 between 35 kK and 37.5 kK.

However, the atmosphere of LP26 is yet to be modelled by means of quantitative spectroscopy, nor has its mass-loss rate been investigated. In this project, we analyse the FUV spectrum of LP26 and run a grid of models using the stellar atmosphere code FASTWIND to determine upper limits of $\dot{M}$ from the C IV $\lambda 1550$ resonance line. These upper limits are then compared to the theoretical predictions of Vink et al. (2001), Krtička and Kubát (2018), and Björklund et al. (2021). The goal of the project is to perform the lowest metallicity test of RDWT to date.

This report is organised as follows. Section 2 describes how the spectrum was obtained; Section 3 outlines the methodology of the project; Section 4 reveals the results obtained; Section 5 provides a discussion of the results and compares them with those from previous works, and conclusions are made in Section 6.

2. Observations

The FUV spectrum of LP26 was obtained by Telford et al. (2021) and was kindly provided by the author to carry out this project. It was taken at medium-resolution ($R \sim 6000$) using G130M and G160M filters of the Cosmic Origins Spectrograph (COS) on the HST in Cycle 27 over the period 10 April, 2020, and 16 June, 2020. To increase the signal-to-noise ratio (SNR), multiple spectra taken over different visits were coadded to produce a single spectrum. The spectrum was then binned into 12Å bins and corrected for foreground extinction using $R_V = 3.1$ and $A_V = 0.04$.

Once obtained, we corrected the spectrum for the radial velocity of LP26, $283\,\text{km}\,\text{s}^{-1}$ (Telford et al., 2021). Due to strong nebular contamination, and a modest average SNR of ~ 9, only two lines
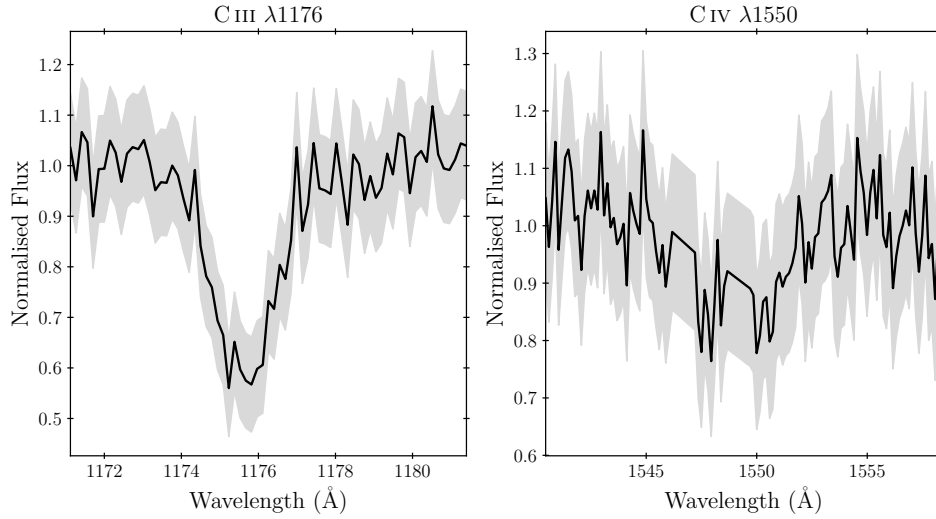
Figure 1. The C IV λ1550 and C III λ1176 lines analysed in this work. The grey shaded regions represent the measurement errors. The lines were normalised according to the method described in Telford et al. (2021), and the interstellar absorption features in the centre of the C IV λ1550 feature were manually clipped.

were identified as suitable for quantitative analysis: the resonant C IV λ1550 line, and the photospheric C III λ1176 line. These lines were then normalised using the same method as Telford et al. (2021), which involves determining bins blue- and redward of the line feature, fitting a line through the points in these bins to determine the continuum, and then dividing the spectrum by this continuum value. Finally, the nebular absorption in the centre of the C IV λ1550 feature was manually clipped. The resulting spectral lines that were used for analysis in this project are shown in Figure 1.

3.   Methods

The modelling of the atmosphere of LP26 was carried out using the stellar atmosphere code FASTWIND (V10.6; Santolaya-Rey et al., 1997; Puls et al., 2005; Rivero González et al., 2012; Carneiro et al., 2016; Sundqvist and Puls, 2018). This is a 1-dimensional NLTE stellar atmosphere code tailored for modelling luminous OBA stars with winds. It solves the equation of hydrostatic equilibrium in spherical symmetry to determine the velocity field in the photosphere, which is then connected to the wind outflow. The

wind is described by a β-type velocity law, which is used, along with the input value for $\dot{M}$, to determine the density structure in the wind. Importantly, FASTWIND takes inhomogeneities in the wind into account by means of a clumping factor. It then calculates the number density rate equations for the "explicit" elements (those for which model atoms are implemented and whose abundances are specified by the user; C, N, O, Si, P) by solving the radiative transfer equation in the comoving frame for each line transition, while it uses the Sobolev approximation to calculate those of the "background" elements. The generated lines are then convolved with the observed rotational velocity, $v_{\rm rot} \sin i$, and the spectral resolution, R, in order to match the observed line profiles. For this work, $v_{\rm rot} \sin i = (370 \pm 90) \, {\rm km \, s^{-1}}$, and $R \sim 6000$ (Telford et al., 2021).

Although carbon lines of two different ionisation stages are available for analysis, the C IV λ1550 is a resonant line and is therefore very sensitive to $\dot{M}$. Consequently, it is not possible to uniquely determine $T_{\rm eff}$, g, or the surface carbon abundance, [C], as there is only one photospheric line available for analysis, namely, the C III λ1176 line.

As a solution to this, a grid of models was cal-

culated to determine optimal values for T_{eff} and $\log(g)$ at different [C], namely $0.01\,\text{C}_\odot, 0.03\,\text{C}_\odot$, and $0.05\,\text{C}_\odot$, where $\text{C}_\odot \equiv \log(N_{C,\odot}/N_{H,\odot}) + 12 = 8.43$ is the surface carbon abundance of the Sun (Asplund et al., 2009). The grid considers eight evenly spaced values of T_{eff} between $33\,\text{kK}$ and $44\,\text{kK}$, and five evenly spaced values of $\log(g)$ between 3.42 and 4.42. These were chosen based off the values and uncertainties determined by Telford et al. (2021).

The motivation behind choosing three values for [C] is because the carbon abundance of LP26 may not be a simply scaled value of the solar value by its metallicity ($Z_{\text{LP26}} \sim 0.03\,\text{C}_\odot$; the nebular value measured by Skillman et al., 2013). For example, Crowther et al. (2022) average the abundances of different elements in the LMC obtained in different works and find that they do not scale by the metallicity of the galaxy ($\sim 0.5 Z_\odot$).

FASTWIND also requires $R_\star$ as an input parameter. This was constrained using HST photometry obtained by McQuinn et al. (2015) during the HST programme GO-13376. These observations were carried out using the Advanced Camera for Surveys (ACS) instrument over the period 23 to 26 April, 2014. We chose to use the magnitude in the F814W filter because of its small uncertainty and that its wavelength range lies well into the Rayleigh-Jeans regime of the SED of LP26. Using this approximation, the radius is given by

$$R_\star = \sqrt{\frac{d^2 \lambda^4 \mathcal{F}_0 10^{-0.4 m_{\text{F814W}}}}{2\pi c k_B T_{\text{eff}}}}, \qquad (1)$$

where $d = (1.62 \pm 0.15)\,\text{Mpc}$ is the distance to Leo P, $m_{\text{F814W}} = 21.929 \pm 0.004$ is the magnitude of LP26 in the F814W HST filter (McQuinn et al., 2015), $\lambda = 8100.44\,\text{Å}$ is the reference wavelength of the filter, and $\mathcal{F}_0 = 1.1132 \times 10^{-9}\,\text{erg cm}^{-2}\,\text{s}^{-1}\,\text{Å}^{-1}$ is the zero point flux in the Vega system for this filter[1].

For each $[\text{C}] - g - T_{\text{eff}}$ grid point, the chi-squared statistic (χ^2) was calculated between the C III $\lambda 1176$ line and the model line. The details of this method are discussed in Section 3.1. Figure 2 shows an exam-

ple of this analysis. From this, an optimal T_{eff} value and corresponding 1σ confidence intervals (CIs) were determined. Repeating this process results in an optimal T_{eff} value for each $[\text{C}] - g$ pair.

Next, upper limits for the value of $\dot{M}$ for these optimal models were calculated using FASTWIND by starting at a low value for $\dot{M}$ as an input parameter (which was $5 \times 10^{-10}\,M_\odot\,\text{yr}^{-1}$), and then gradually increasing it until the χ^2 value changed by a significant amount. Figure 3 shows an example of how the 3σ upper limit was determined for $[\text{C}] = 0.05\,\text{C}_\odot$ and $\log(g/\text{cm s}^{-2}) = 3.67$. These upper limits were then compared to a number of different theoretical predictions; namely, those of Vink et al. (2001), Krtička and Kubát (2018), and Björklund et al. (2021). A brief description of each recipe, as well as their formulae, is provided in Appendix A.

The spectral analysis does not allow us to select the most optimal model from the set of optimal models, however, due to the degeneracy between T_{eff} and $\log(g)$ for a given [C] (discussed in Section 4.1; see Figure 4). The range of possible gravities implies a range in possible masses, to which we refer as spectroscopic masses M_{spec} as they result from our spectral analysis. In order to break the degeneracy, we compare the optimal models to stellar evolution tracks from the "dwarfB" grid ($Z/Z_{\text{MW}} \sim 1/25$) of the Bonn Optimised Stellar Tracks (BoOST; Szécsi et al., 2022), and require $M_{\text{evol}} = M_{\text{spec}}$, where M_{evol} is the evolutionary mass that we constrain from placing the star (model) in the Hertzsprung-Russel (HR) diagram. If the position of the model on the HR diagram is located far from the track of a star of the same M_{evol}, we conclude that it is unlikely for a star with this M_{spec} to exist, and therefore rule it out. This is discussed further in Section 4.3. Consistently, throughout this report, we will refer to either M_{spec} or M_{evol}, where appropriate.

3.1. Chi-Squared Fitting

As discussed above, chi-squared fitting is performed to determine optimal parameters. The chi-squared

---

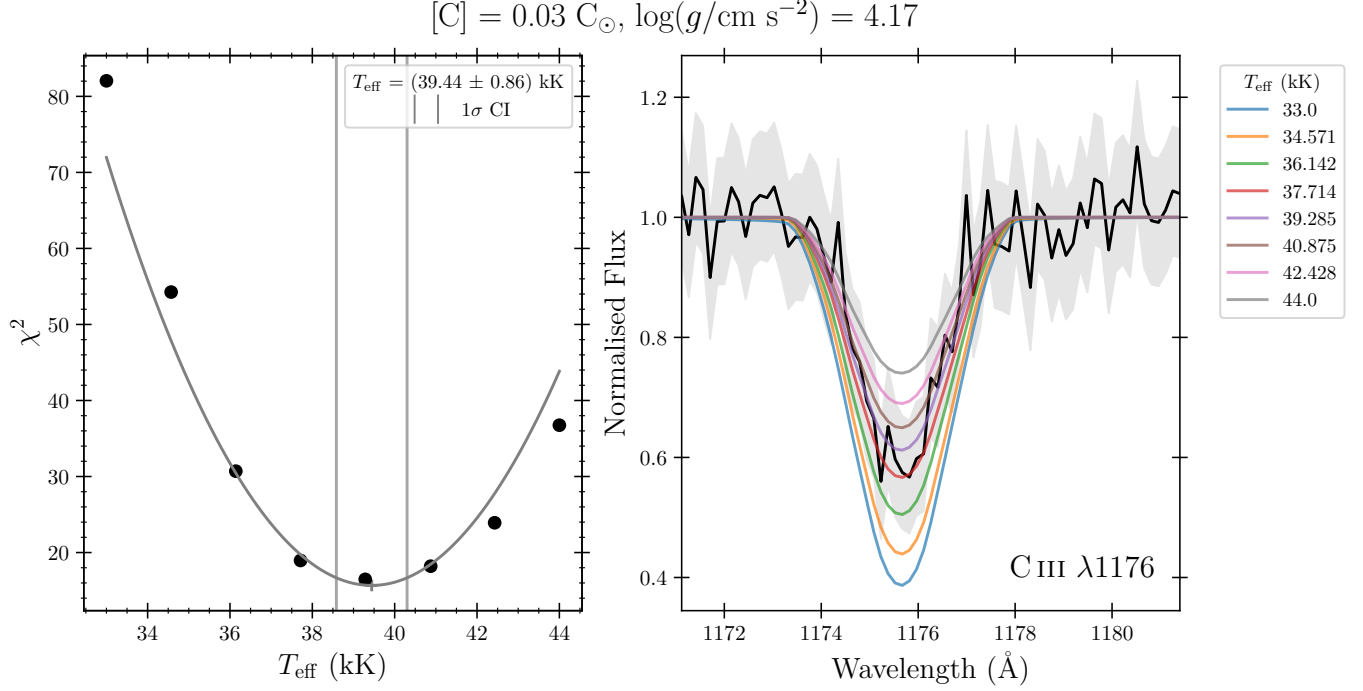[1]Values for λ and $\mathcal{F}_0$ were obtained from the Filter Profile Service, accessed 17 March, 2023.

Figure 2. Example of the determination of the optimal T_{eff} value for $\log(g/\mathrm{cm\,s^{-2}}) = 4.17$ and $[\mathrm{C}] = 0.03\,\mathrm{C_\odot}$. Here, a parabola is fit around the minimum of the χ^2 curve and the optimal T_{eff} value is taken to be the minimum of this parabola. The 1σ CI is determined using Equation (3) for $\nu = 1$.
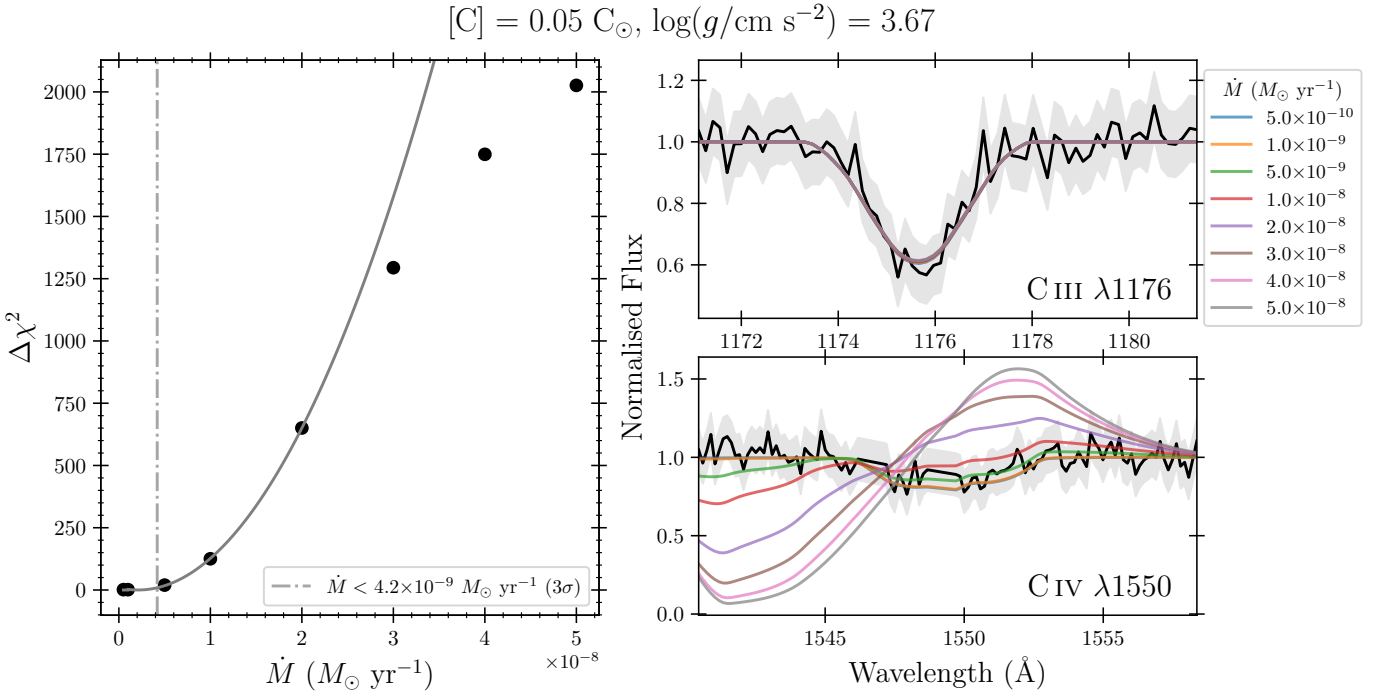

Figure 3. Example of the determination of the upper limit of $\dot{M}$ for $\log(g/\mathrm{cm\,s^{-2}}) = 3.67$ and $[\mathrm{C}] = 0.05\,\mathrm{C_\odot}$. The χ^2 statistic is calculated on both carbon lines to ensure any differences in the C III $\lambda1176$ line due to stellar winds are captured. Again, a parabola is fit around the minimum of the χ^2 surface and then the value $\Delta\chi^2 = \chi^2 - \chi^2_{\mathrm{min}}$ as a function of $\dot{M}$ is plotted, because it is the change in χ^2 that matters in the determination of upper limits.

statistic for a model of some parameter θ is given by

$$\chi^2(\theta) = \sum_{i=1}^{N} \left(\frac{\mathcal{F}(\lambda_i) - \mathcal{F}_{\mathrm{mod}}(\lambda_i; \theta)}{\sigma_i} \right)^2, \qquad (2)$$

where $\mathcal{F}(\lambda_i)$ is the observed flux at wavelength λ_i with an uncertainty σ_i, and $\mathcal{F}_{\mathrm{mod}}(\lambda_i; \theta)$ is the model flux at λ_i. Technically, θ is a vector composed of all of the input parameters to FASTWIND, however, for both the determination of the optimal T_{eff} and the upper limits for $\dot{M}$, only these parameters are varying in each case. Even though $R_\star$ is varying in the determination for T_{eff}, it is dependant on T_{eff} by Equation (1) and is therefore not a free parameter.

Since a relatively sparse grid of T_{eff} values were calculated, a parabola was fit to the minimum of the χ^2 curve. The reasoning for this is two fold. Firstly, it roughly provides the shape of the curve that would be generated if more models were calculated, meaning that the optimal value for T_{eff} can be approximated by the minimum of this parabola. Second, if the real χ^2 values resemble this parabola well enough, this means that they can be approximated as being normally distributed, meaning that CIs may be estimated. The $n\sigma$ CI is located at $\pm\Delta\theta$ from the optimal parameter $\hat{\theta}$ where

$$\chi^2(\hat{\theta} \pm \Delta\theta) - \chi^2(\hat{\theta}) = F_{\chi^2_\nu}^{-1}(P(n\sigma)), \qquad (3)$$

where $F_{\chi^2_\nu}^{-1}(P(n\sigma))$ is the inverse cumulative density function of the probability of $n\sigma$ for the chi-squared distribution with ν degrees of freedom. Since, for both cases, only one parameter is varying, $\nu = 1$ and therefore $F_{\chi^2_{\nu=1}}^{-1}(P(n\sigma)) = n^2$. Therefore, the $n\sigma$ confidence interval is located at the parameter $\Delta\theta$, whose value of χ^2 is n^2 greater than that of $\hat{\theta}$. This analysis can be extended to upper limits, where the $n\sigma$ upper limit is determined by Equation 3 for $\nu = 1$.

4.   Results

4.1.   Optimal models

Figure 4 shows, for each [C], the χ^2 surface for the $\log(g) - T_{\mathrm{eff}}$ grid. The surfaces have been interpolated for clarity. What is immediately apparent is a

"valley" of degeneracy, between $\log(g)$ and T_{eff}; that is, for each value of $\log(g)$, a different value of T_{eff} is optimal, and this value is higher for higher values of $\log(g)$. Each of these optimal values are represented by the black points in Figure 4. The physical parameters of these optimal models are given in Table 1, where M_{spec} and L were calculated using

$$M_{\mathrm{spec}} = \frac{gR_\star^2}{G}, \qquad (4)$$

$$L = 4\pi R_\star^2 \sigma T_{\mathrm{eff}}^4, \qquad (5)$$

respectively. It is important to note that the uncertainties determined for T_{eff} do not account for the uncertainty introduced by fixing $\log(g)$, and are therefore underestimates of the true uncertainties. This has important implications when comparing the results obtained in this work to previous results, which is discussed further in Section 5.

The uncertainties on $R_\star$, M_{spec}, and L were estimated using error propagation, where the uncertainties on d and T_{eff} were propagated to determine those of $R_\star$, which were then used to determine the uncertainties for M_{spec} and L. The uncertainty on the F814W magnitude was neglected here. However, as mentioned above, since the uncertainty values for T_{eff} are underestimates, this implies uncertainties on all other quantities are also lower than their true values.

This approximation requires that each of the parameters are uncorrelated. This is the case for the determination of the uncertainty on $R_\star$, and consequently those on M_{spec}, as d and T_{eff} are not correlated. On the other hand, since L depends on both T_{eff} and $R_\star$, the estimate of the uncertainties on L are technically a lower limit, as there would be extra contributions from correlations between T_{eff} and $R_\star$. Inspection of the uncertainties on $R_\star$ reveals that they are dominated by the uncertainty on the distance to Leo P over the uncertainties on T_{eff} by a factor of ~ 9000. Therefore, contributions from correlation terms between T_{eff} and $R_\star$ are negligible compared to the contribution by the radius uncertainty, thus making the uncertainty estimates for L reasonable. In fact, this also means that all other uncertainty es-
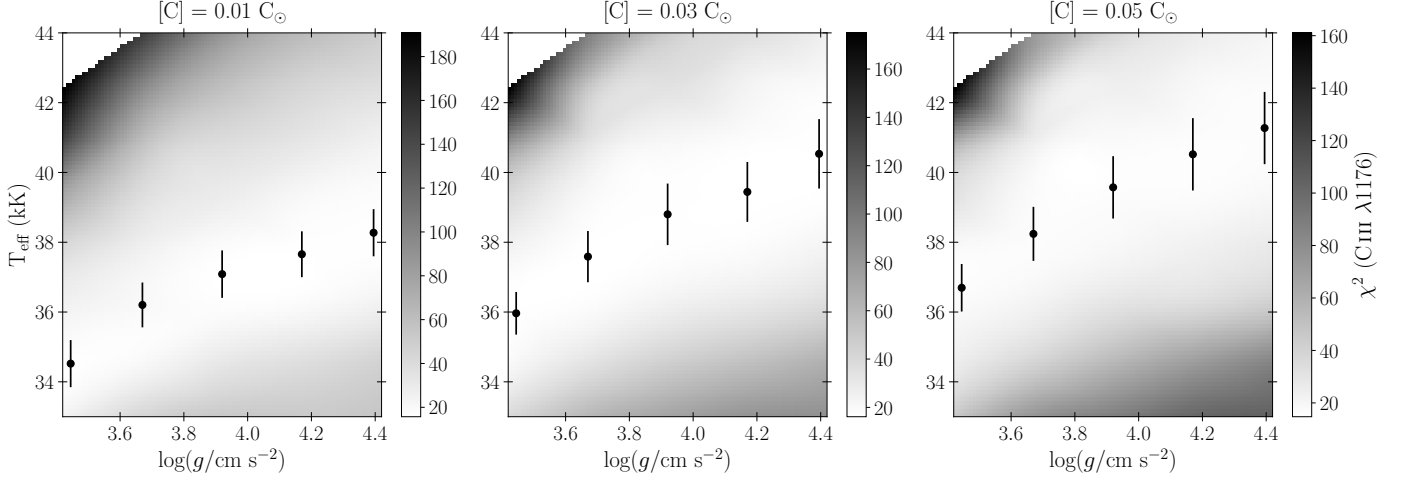
Figure 4. The interpolated χ^2 surfaces of the $T_{\mathrm{eff}} - \log(g)$ grid for each [C] analysed. The black points represent the optimal T_{eff} values and corresponding 1σ CIs for each [C]$-\log(g)$ pair. The shading of the surface is mapped to the value of χ^2, where light to dark shading represents low to high χ^2 values. On each plot, the points of highest and lowest $\log(g)$ have been moved in, for clarity, by -0.025 and +0.025, respectively.

timates are reasonable, even though the uncertainties on T_{eff} have been underestimated, because these all depend on the radius uncertainty which is dominated by the distance uncertainty.

4.2. Upper limits for $\dot{M}$

Figure 5 shows the 1σ and 3σ upper limits of $\dot{M}$ for each of the models in Table 1. As well as this, it shows the predictions of Vink et al. (2001), Krtička and Kubát (2018), and Björklund et al. (2021) for these models, whose values are given by Equations (6), (7), and (8), respectively. It can be seen that, for the highest L model, each prediction is below the determined upper limits. This is also the case for the next highest L model, apart from the predictions of Vink et al. (2001), as these lie within the uncertainties on L for these models. For the three lowest L models, the Vink et al. (2001) rate overpredicts $\dot{M}$, and the Krtička and Kubát (2018) overpredicts that of the lowest L model.

4.3. Comparison with BoOST Models

Although Figure 5 suggests that theory is incorrectly predicting the upper limit of $\dot{M}$ for some models, there is still the question whether or not stars of

these parameters are likely to exist, based on our current understanding of stellar evolution. To answer this, the models were compared to evolutionary tracks from the Bonn Optimized Stellar Tracks (BoOST; Szécsi et al., 2022) models. Figure 6 shows the models of each [C] plotted on the HR diagram along with interpolated evolutionary tracks from the "dwarfB" grid ($Z/Z_{\mathrm{MW}} \sim 1/25$). The tracks shown are those whose evolutionary mass M_{evol} is closest to the spectroscopic mass M_{spec} of the optimal models. The tracks closest in mass to the two lowest mass models are not shown because the lowest mass interpolated BoOST track is $9\,M_{\odot}$, and it would also be at much lower values of $\log(L/L_{\odot})$ on the HR diagram, therefore they have been neglected for clarity.

Figure 6 demonstrates how some of the optimal models may be ruled out. For each carbon abundance, the optimal model with the highest M_{spec} and the three lowest M_{spec} models are all far from where stars of these masses are expected to evolve in the HR diagram. Instead, they have L and T_{eff} of a main sequence star of $\sim 20\,M_{\odot}$ at this metallicity. Table 1 shows M_{evol} of these suboptimal models; that is, the mass of the evolutionary track to which these models are closest to on the HR diagram. It can be seen that M_{spec} of these models are far from their M_{evol}.
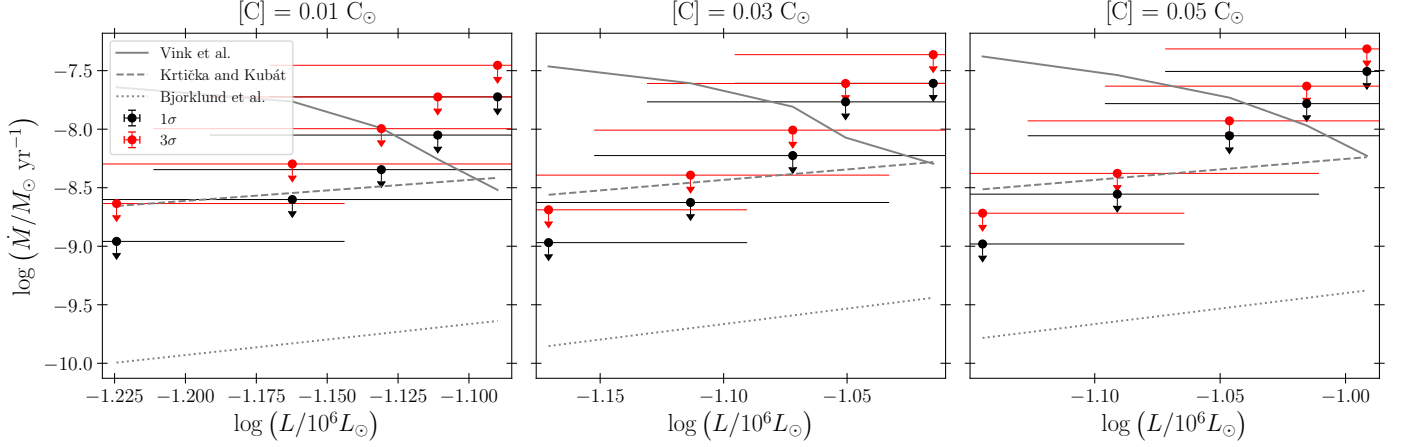
Figure 5. The 1σ (black points) and 3σ (red points) upper limits of $\dot{M}$ of the optimal models as a function of $\log(L/10^6 L_\odot)$. Also shown are the predictions of Vink et al. (2001), Krtička and Kubát (2018), and Björklund et al. (2021) (solid, dashed, and dotted lines, respectively) for $\dot{M}$ of these optimal models.
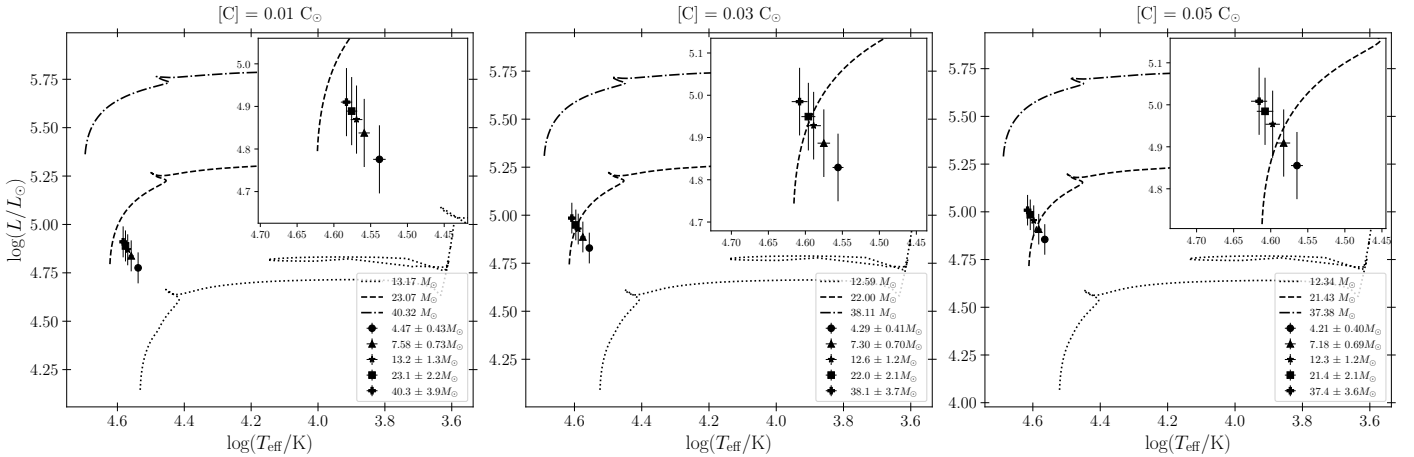

Figure 6. The optimal models plotted on the HR diagram along with the BoOST tracks with M_{evol} closest to M_{spec} of the three most massive optimal models. Shown on each plot is a the zoomed-in section of the region in the HR diagram where the optimal models lie.
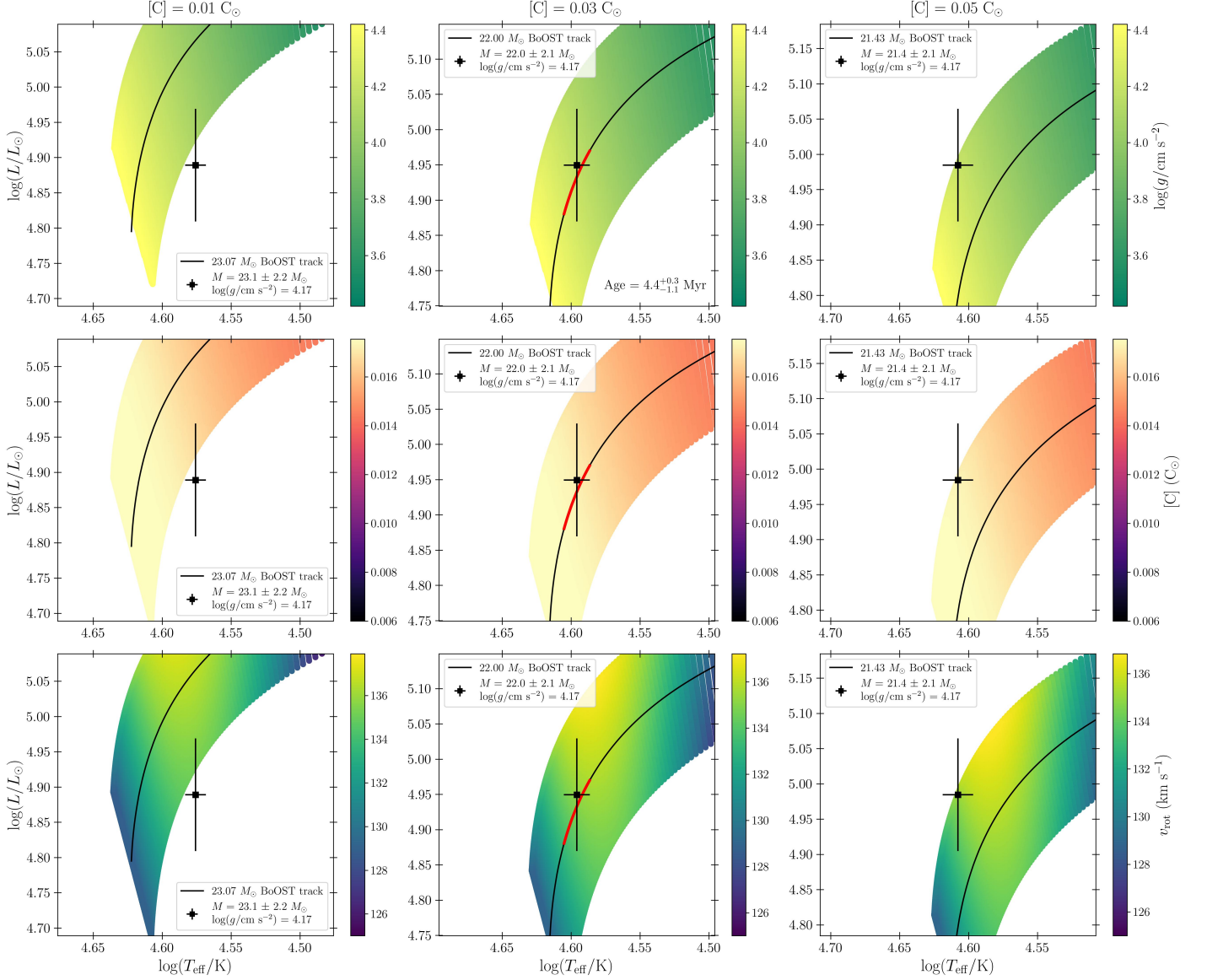
Figure 7. The models of $M_{\rm spec} \sim 20\,M_\odot$ for each [C] plotted alone on the HR diagram along with the BoOST track $M_{\rm evol} = M_{\rm spec}$ (black line) and all BoOST tracks with $M_{\rm evol}$ within the uncertainties of $M_{\rm spec}$ of the model (shaded regions). Each column represents a different value for [C], and each row represents different quantities of the BoOST tracks, whose colours are mapped to the values on the colour bar. From top to bottom, the quantities shown are $\log(g)$, [C] of the BoOST models, and the rotational velocity of the BoOST tracks, $v_{\rm rot}$. For the [C] = $0.03\,{\rm C}_\odot$ model, given how well it is represented by its corresponding BoOST track, the region on the BoOST track that lies within the L and $T_{\rm eff}$ uncertainties is plotted in red, which is then used to estimate the age of LP26, shown in the bottom-right corner of the centre plot on the top row.

Therefore, it is unlikely that these models represent LP26, and can be ruled out as a result.

To further analyse the most likely models (those of $M_{\text{spec}} \sim 20\,M_\odot$ or $\log(g) = 4.17$), they are plotted alone in Figure 7 along with the BoOST track that is closest to them in M_{evol}, as well as all BoOST tracks with M_{evol} within the uncertainties of the M_{spec} of the model. Each column represents the different values for [C] tested in this work, and each row shows different quantities of the BoOST models. From top to bottom, these are $\log(g)$, [C], and the rotational velocity of the BoOST tracks, v_{rot}, and their values are mapped to the colour of the shading in the plot.

The interpolated BoOST models provide the surface mass fractions of elements, so that of C had to be converted into surface abundance in the standard notation. For element X, the surface abundance is $\log(\epsilon_X) = \log(N_X/N_{\text{H}}) + 12$, where N_{H} is the surface hydrogen abundance. If the surface mass fraction of element X is M_X, then $N_X = M_X/m_X$, where m_X is the mass of an atom of element X. Then the surface abundance of X expressed as a fraction of the solar value is like $10^{\log(\epsilon_X) - \log(\epsilon_{X,\odot})}$. This had to be carried out for both C and H, and $\log(\epsilon_{C,\odot}) = 8.43$ (Asplund et al., 2009). The results of this conversion is what is quoted in Figure 7.

Firstly, the models of $0.01\,\text{C}_\odot$ and $0.05\,\text{C}_\odot$ are not very well represented by the BoOST tracks of the same M_{evol}. The upper limits on L, and consequently M_{spec}, for the $0.01\,\text{C}_\odot$ model lie in the lower limits of the mass range of the BoOST models, and vice-versa for the $0.05\,\text{C}_\odot$ model. M_{evol} for these two models are quoted in Table 1.

On the other hand, the $0.03\,\text{C}_\odot$ model with $M_{\text{spec}} = (22.0 \pm 2.1)\,M_\odot$ is extremely well represented by the BoOST track of the same mass, as the point lies almost directly on the track. Therefore, we take this to be the most optimal model. The age of LP26 may be estimated by taking it to be the time of the simulation of the closest point on the BoOST track to where the model is on the HR diagram, and the uncertainty is estimated by the region within the model

uncertainties on L and T_{eff}. This region is plotted on the evolutionary track in red, and doing this gives an age estimate for LP26 of $4.4^{+0.3}_{-1.1}\,\text{Myr}$. This is consistent with a main sequence O dwarf, which matches with previous age determinations for LP26.

Examining the $0.03\,\text{C}_\odot$, $(22.0 \pm 2.1)\,M_\odot$ model further, we can see that its value for $\log(g)$ is consistent with those of the BoOST models, which, according to the colour, is $\sim 4.1, 4.2$. On the other hand, for the BoOST models, $v_{\text{rot}} \sim 134\,\text{km s}^{-1}$, which is lower than that of LP26, and the surface carbon abundance is $\sim 0.016\,\text{C}_\odot$, roughly half that of the optimal model. These discrepancies are discussed in Section 5.

5. Discussion

5.1. Comparison with previous work

The parameters of the most optimal model are highlighted in Table 1. They are, for the most part, in good agreement with those obtained by Telford et al. (2021) from their SED fit, even though a completely different approach was taken here to determine them. The age (quoted on the top-middle panel of Figure 7), M_{spec}, $\log(g)$, and $\log(L/L_\odot)$ are equal within uncertainties, however, there are discrepancies between the value obtained for $R_\star$, and with the value for T_{eff} obtained by Telford et al. (2023).

5.1.1. Temperature Discrepancy

As for T_{eff}, Telford et al. (2023) constrain it to be between $35\,\text{kK}$ and $37.5\,\text{kK}$ using nebular emission lines together with CLOUDY photoionisation models. They relate the emission line fluxes of the nebular Hβ and the He I $\lambda 4471$ emission lines to the total H- and He-ionising photon production rates ($Q(\text{H})$ and $Q(\text{He})$, respectively) and find a ratio of $Q(\text{He})/Q(\text{H}) = 0.12 \pm 0.03$. They then compared this to values of this quantity produced by TLUSTY (Hubeny and Lanz, 1995) spectral models from the OSTAR2002[2] grid. They find that, within the 2% $Z_\odot$, $\log(g/\text{cm s}^{-2}) = 4.00$ grid, the models

---

[2]http://tlusty.oca.eu/Tlusty2002/tlusty-frames-OS02.html

with $T_{\text{eff}} = 35\,\text{kK}$ and $37.5\,\text{kK}$ produce $Q(\text{He})/Q(\text{H})$ of 0.09 and 0.18, respectively. From this, they conclude that T_{eff} for LP26 should lie within this range.

The methodology applied by Telford et al. (2023) is prone to systematic uncertainties related to assumptions in the methodology, as is the case in our work. Important ones are the geometry of the H II region, which is assumed to have a plane-parallel geometry in the CLOUDY models. As well as this, they adopt an escape fraction $f_{\text{esc}} = 0$ in the calculation of $Q(\text{H})$ and $Q(\text{He})$ because the H II region is isolated and almost perfectly spherical in shape, and because they detect low-ionisation [S II] emission in the outer regions of the nebula, implying that the H II region is optically thick to ionising photons. In reality, however, there may be inhomogeneities in the geometry of the H II region, and some ionising photons may escape the nebula, which would result in a f_{esc} slightly greater than 0. This would result in higher $Q(\text{H})$ and $Q(\text{He})$ values, and, consequently, a higher T_{eff} for LP26.

With this nebular constraint, we turn to T_{eff} determined in this work, which was $(39.44 \pm 0.86)\,\text{kK}$. This value does not lie within the limits set by Telford et al. (2023). However, as mentioned in Section 4.1, these uncertainty estimates are lower than the true values, as they do not account for the uncertainty in fixing $\log(g)$. If this was accounted for, the uncertainties should increase and result in a closer match with the results of Telford et al. (2023).

As well as this, it is important to note that Telford et al. (2023) used a grid where $\log(g/\text{cm}\,\text{s}^{-2}) = 4.00$. The optimal model determined in this work has $\log(g/\text{cm}\,\text{s}^{-2}) = 4.17$. As demonstrated by Figure 4, while there is a degeneracy between $\log(g)$ and T_{eff}, there is also a positive correlation between them. It could be, therefore, that the best matching TLUSTY models from the region of the OSTAR2002 grid with a higher $\log(g)$ would result in different values for T_{eff} in order to match the observed $Q(\text{He})/Q(\text{H})$. Follow up confirmation of this would prove useful.

Furthermore, close examination of Figure 2, which shows how this optimal T_{eff} was determined,

reveals that the model of $\sim 37.7\,\text{kK}$ is also a good representation of the C III $\lambda 1176$ line. This model accurately matches the depth of the line, while the optimal model of $\sim 39\,\text{kK}$ more accurately represents the wings of the line. Since there are more data points in the wings of line, the χ^2 minimisation algorithm favours the hotter model. For the purpose of this project, we favour the model with the lowest χ^2 value, and, given the quality of the data, a more effective method to achieve the goals of this project than what was carried out here could not be determined.

This issue would be resolved if there were more photospheric lines suitable for modelling as opposed to only one. For example, a carbon line from another ionisation stage would constrain the temperature much more accurately. This is an inherent uncertainty associated with this project. Follow-up FUV observations of LP26 consisting of more and longer exposures than those taken by Telford et al. (2021) would result in a higher signal coadded spectrum, thus potentially revealing more photospheric lines.

5.1.2. Radius discrepancy

The radius of the optimal model for this work is $(6.39 \pm 0.59)\,R_\odot$, which was determined using the magnitude of LP26 in the F814W filter and the Rayleigh-Jeans approximation of the blackbody formula, while Telford et al. (2021) obtained a value of $8.2^{+1.3}_{-0.4}R_\odot$, which, along with all other parameters, was determined using the TLUSTY OSTAR2002 grid.

Since $R_\star$ is not sampled in this grid, for each value of T_{eff} and $\log(g)$ in a grid of a certain Z, they determine the corresponding $R_\star$ from the PARSEC stellar evolution models of these parameters. Then for each of these values, as well as a certain extinction law, R_V, they optimise a parameter that describes the dust extinction towards LP26, A_V, and one that quantifies the nebular contribution to the SED, $f_{\text{FUV}}^{\text{nebular}}$. They then perform chi-squared minimisation on this grid point with the optimised values for A_V and $f_{\text{FUV}}^{\text{nebular}}$, and the optimal set of parame-

ters at this Z and R_V was taken as those with the lowest χ^2 value. Finally, optimal Z and R_V were determined by visual inspection.

After discussion with the author of this work, the nature of the discrepancy between the two radius values remains unclear, although a couple of possibilities were brought up. Firstly, there could be degeneracies in optimisation of both A_V and $f_{\mathrm{FUV}}^{\mathrm{nebular}}$ which would result in different preferred properties of LP26 for different, equally optimal $A_V - f_{\mathrm{FUV}}^{\mathrm{nebular}}$ pairs. Second, the PARSEC models that were used to determine $R_\star$ for a $T_{\mathrm{eff}} - \log(g)$ grid point were non-rotating, while it has been found that LP26 has a significant rotational velocity $v_{\mathrm{rot}} \sin i \sim 370\,\mathrm{km\,s^{-1}}$, so this could also affect the true value for $R_\star$. Further investigation into the nature of this discrepancy would prove to be beneficial as we look to accurately characterise the nature of the XMP LP26.

5.2. Discrepancies with the BoOST models

Figure 7 demonstrates a remarkable match between the model with $[\mathrm{C}] = 0.03\,\mathrm{C_\odot}$ and $M_{\mathrm{spec}} = (22.0 \pm 2.1)\,M_\odot$ and the interpolated BoOST track of equal M_{evol}. However, as noted in Section 4.3, there is a discrepancy between v_{rot} and $[\mathrm{C}]$ of the BoOST tracks and the optimal model, which are both a factor of roughly a half lower in the BoOST models.

The lower rotational velocity is because the BoOST models begin their lives at an initial $v_{\mathrm{rot}} = 100\,\mathrm{km\,s^{-1}}$. However the origin of the lower surface carbon abundances in the BoOST models is unclear. A possible cause may be due to uncertainties in the adopted rotation-induced mixing efficiency in the BoOST models. Future work examining effects of rotation on the surface abundances in stellar evolution models of low metallicity massive stars would be beneficial in determining whether this could be a valid reason.

5.3. The test of RDWT

Taking the parameters of the most optimal model as the most likely description of LP26, then, as demonstrated by the second most luminous model in the

centre plot of Figure 5, each theoretical formula successfully predicts a value of $\dot{M}$ lower than both the 1σ and 3σ upper limits determined from the chi-squared fit. Therefore, RDWT is consistent with the results obtained in this work. This means that this project is the lowest metallicity test of RDWT to date.

6. Conclusions

In this project, we analysed the FUV spectrum of the XMP O dwarf LP26 as we looked to perform the lowest metallicity test of radiation-driven wind theory (RDWT) to date. We used FASTWIND to run a grid of models to find optimal values for T_{eff} for different $[\mathrm{C}] - \log(g)$ pairs based off the photospheric C III λ1176 line. Upper limits for $\dot{M}$ for these optimal models were then calculated using the C IV λ1550 line, and were compared to a number of theoretical predictions. To converge on a single optimal description of the parameters of LP26, the models were compared to the interpolated evolutionary tracks of stars of the same mass from the "dwarfB" grid of the BoOST models. It was found that the model with $[\mathrm{C}] = 0.03\,\mathrm{C_\odot}$, $M_{\mathrm{spec}} = (22.0 \pm 2.1)\,M_\odot$ provides the most accurate description of LP26 due to its excellent alignment on the HR diagram with the BoOST model with the same M_{evol} as M_{spec}. We estimate the age of LP26 to be $4.4^{+0.3}_{-1.1}$ Myr. We find that each theoretical prediction of $\dot{M}$ of this optimal model successfully predicts values below both the 1σ and 3σ upper limits.

The parameters of this optimal model also match up nicely with results obtained in previous works that use alternative methods, although there are a couple of discrepancies, the sources of which are not known exactly but are discussed in Section 5. This is still a remarkable result, given only two spectral lines were available for analysis. Follow up FUV spectroscopy of LP26 consisting of taking more spectra with longer exposures would result in a higher signal coadded spectrum, which could potentially reveal more photospheric lines of LP26 suitable for analysis. This would allow for more conclusive quantitative spectroscopy to be carried out. Furthermore, closer anal-

ysis of the discrepancies between the results obtained in this work and previous work would prove beneficial as we look to learn more about the nature of massive XMP O stars, and consequently, the very first stars in the Universe.

References

Asplund, M., Grevesse, N., Sauval, A. J. and Scott, P. (2009), *ARA&A* **47**, 481–522.

Björklund, R., Sundqvist, J., Puls, J. and Najarro, F. (2021), *A&A* **648**, A36.

Bosman, S. E., Davies, F. B. et al. (2022), *MNRAS* **514**(1), 55.

Carneiro, L. P., Puls, J., Sundqvist, J. and Hoffmann, T. (2016), *A&A* **590**, A88.

Castor, J. I., Abbott, D. C. and Klein, R. I. (1975), *APJ* **195**, 157–174.

Crowther, P. A., Broos, P. S., Townsley, L. K. et al. (2022), *MNRAS* **515**(3), 4130–4150.

Hirano, S., Hosokawa, T. et al. (2014), *APJ* **781**(2), 60.

Hubeny, I. and Lanz, T. (1995), *APJ* **439**, 875–904.

Krtička, J. and Kubát, J. (2018), *A&A* **612**, A20.

McQuinn, K. B., Skillman, E. D. et al. (2015), *APJ* **812**(2), 158.

Mokiem, M., de Koter, A., Vink, J. et al. (2007), *A&A* **473**(2), 603–614.

Puls, J., Urbaneja, M., Venero, R. et al. (2005), *A&A* **435**(2), 669–698.

Rivero González, J. G., Puls, J., Najarro, F. and Brott, I. (2012), *A&A* **537**, A79.

Santolaya-Rey, A., Puls, J. and Herrero, A. (1997), *A&A* **323**, 488–512.

Skillman, E. D., Salzer, J. J. et al. (2013), *APJ* **146**(1), 3.

Sundqvist, J. and Puls, J. (2018), *A&A* **619**, A59.

Szécsi, D., Agrawal, P., Wünsch, R. and Langer, N. (2022), *A&A* **658**, A125.

Telford, O. G., Chisholm, J., McQuinn, K. B. and Berg, D. A. (2021), *APJ* **922**(2), 191.

Telford, O. G., McQuinn, K. B., Chisholm, J. and Berg, D. A. (2023), *APJ* **943**(1), 65.

Vink, J. S. (2022), *ARA&A* **60**, 203–246.

Vink, J. S., de Koter, A. and Lamers, H. (2001), *A&A* **369**(2), 574.

Wise, J. H. (2019), *Contemporary Physics* **60**(2), 145–163.

A.   The different mass-loss recipes

In this section, the equations of the different $\dot{M}$ predictions are provided. Firstly, there is that of Vink et al. (2001). This was derived using global energy conservation arguments and Monte Carlo methods. Neglecting the uncertainties for clarity, this gives

$$
\begin{aligned}
\log \dot{M} = & -6.697 \\
& + 2.194 \log(L/10^5 L_\odot) \\
& - 1.313 \log(M/30 M_\odot) \\
& - 1.226 \, \log\left(\frac{v_\infty/v_{\mathrm{esc}}}{2.0}\right) \\
& + 0.933 \log(T_{\mathrm{eff}}/40\,000\,\mathrm{K}) \\
& - 10.92 \{\log(T_{\mathrm{eff}}/40\,000\,\mathrm{K})\}^2 \\
& + 0.85 \log(Z/Z_\odot),
\end{aligned} \tag{6}
$$

for $27\,500\,\mathrm{K} < \mathrm{T}_{\mathrm{eff}} \leq 50\,000\,\mathrm{K}$.

Next, there is the formula of Krtička and Kubát (2018) which was derived by solving the radiative transfer equation, kinetic equilibrium equations, and hydrodynamic equations in the photosphere and the wind, and assumes a stationary and spherically symmetric wind. This gives

$$
\begin{aligned}
\log \dot{M} = & -5.70. + 0.50 \log(Z/Z_\odot) \\
& + [1.61 - 0.12 \log(Z/Z_\odot)] \log(L/10^5 L_\odot).
\end{aligned} \tag{7}
$$

Finally, there is the prediction of Björklund et al. (2021), where they used iterative methods to solve the equation of motion using NLTE radiative transfer in the comoving frame. This formula is

$$
\begin{aligned}
\log \dot{M} = & -1.55 + 0.46 \log(Z/Z_\odot) \\
& + [2.16 - 0.32 \log(Z/Z_\odot)] \log(L/10^5 L_\odot).
\end{aligned} \tag{8}
$$

B.   Optimal model parameters

This section provides a table of the optimal parameters for each $[\mathrm{C}] - \log(g)$ pair obtained from the grid search method. These can be seen in Table 1.

[C] ($C_\odot$)	$\log(g/\mathrm{cm\,s^{-2}})$	T_{eff} (kK)	$R_\star/R_\odot$	$M_{\mathrm{spec}}/M_\odot$	$M_{\mathrm{evol}}/M_\odot$	$\log(L/L_\odot)$
0.01	3.42	34.52 ± 0.67	6.83 ± 0.63	4.47 ± 0.43	17.60	4.776 ± 0.080
0.01	3.67	36.20 ± 0.64	6.67 ± 0.62	7.58 ± 0.73	18.86	4.833 ± 0.080
0.01	3.92	37.09 ± 0.69	6.59 ± 0.61	13.2 ± 1.3	19.74	4.869 ± 0.080
0.01	4.17	37.66 ± 0.66	6.54 ± 0.61	23.1 ± 2.2	20.31	4.889 ± 0.080
0.01	4.42	38.27 ± 0.68	6.49 ± 0.60	40.2 ± 3.9	20.98	4.910 ± 0.080
0.03	3.42	35.96 ± 0.61	6.69 ± 0.62	4.29 ± 0.41	18.70	4.820 ± 0.080
0.03	3.67	37.59 ± 0.73	6.54 ± 0.61	7.30 ± 0.70	20.26	4.886 ± 0.080
0.03	3.92	38.80 ± 0.88	6.44 ± 0.60	12.6 ± 1.2	21.53	4.928 ± 0.080
0.03	4.17	39.44 ± 0.86	6.39 ± 0.59	22.0 ± 2.1	22.00	4.949 ± 0.080
0.03	4.42	40.5 ± 1.0	6.30 ± 0.58	38.1 ± 3.7	23.52	4.985 ± 0.080
0.05	3.42	36.70 ± 0.68	6.62 ± 0.61	4.21 ± 0.40	19.36	4.855 ± 0.080
0.05	3.67	38.23 ± 0.77	6.49 ± 0.60	7.18 ± 0.69	20.88	4.909 ± 0.080
0.05	3.92	39.57 ± 0.89	6.38 ± 0.59	12.3 ± 1.2	22.38	4.954 ± 0.080
0.05	4.17	40.5 ± 1.0	6.30 ± 0.58	21.4 ± 2.1	23.42	4.985 ± 0.080
0.05	4.42	42.3 ± 1.0	6.25 ± 0.58	37.4 ± 3.6	24.35	5.009 ± 0.080

Table 1. Parameters of the optimal models determined from the grid search. The parameters of the most optimal model, as determined by the comparison with the BoOST models, are highlighted. For all but the most optimal model, M_{evol} represents the mass of the BoOST track to which the model is closest to on the HR diagram, while M_{evol} of the most optimal model is the result of our requirement of $M_{\mathrm{spec}} = M_{\mathrm{evol}}$. The uncertainties on T_{eff} were determined by the method discussed in Section 3.1. The corresponding uncertainty estimates on T_{eff} using Equation (3), along with the uncertainty in the distance measurement obtained from McQuinn et al. (2015), were used to estimate the uncertainty on $R_\star$, which was then used to estimate those on M_{spec} and L. The uncertainties for L are dominated by the uncertainty on the distance to Leo P.